PAPER

Check for updates

Mono-, bi- and tri-metallic platinum group metal-free electrocatalysts for hydrogen evolution reaction following a facile synthetic route†

Seyed Ariana Mirshokraee,[a] Mohsin Muhyuddin,[a] Jacopo Orsilli,[a] Enrico Berretti, [iD][b] Laura Capozzoli,[b] Alessandro Lavacchi,[b] Carmelo Lo Vecchio, [iD][c] Vincenzo Baglio,[c] Anna Galli,[a] Andrea Zaffora, [iD][d] Francesco Di Franco,[d] Monica Santamaria, [iD][d] Luca Olivi, [iD][e] Simone Pollastri [iD][ef] and Carlo Santoro [iD]*[a]

In this work, platinum group metal-free (PGM-free) electrocatalysts were synthesized, characterized, and tested for hydrogen evolution reaction (HER). These materials were mono-, bi- and trimetallic Ni-based electrocatalysts with the addition of a second or a third transition metal (TM), such as iron and cobalt. TM–phthalocyanine (TMPc) was used as a metal precursor, mixed with a conductive carbon backbone and subjected to pyrolysis under controlled temperature and atmosphere conditions. Two temperatures of pyrolysis (600 °C and 900 °C) were used. The effect of TM loading in the precursors, different pyrolysis temperatures on the surface chemistry and morphology, and electrocatalytic activity towards HER were evaluated. The increase of NiPc in the initial mixture is beneficial to improving the electrocatalytic activity. The addition of a second and a third metal reflects positively on the HER performance. Interestingly, the pyrolysis temperature influences both the formation and growth of the nanoparticles, and this information is supported by high-resolution transmission electron microscopy (HR-TEM) and light synchrotron X-ray absorption spectroscopy (XAS) measurements.

1 Introduction

Hydrogen with clear-sighted solutions to climate challenges is emerging as a modern energy vector. Owing to its higher power, greater energy density, and negligible contribution to carbon footprint, hydrogen can be regarded as a rational and sustainable fuel. The clean production of hydrogen through water electrolysis can be coupled with renewable energy resources, *i.e.*, wind and solar, that would otherwise lose their practicality due to weather dependency and intermittent disruption. Hence, hydrogen can potentially fuel the automobile, domestic and industrial sectors with zero emissions.[1–3]

Presently, low-temperature water electrolyzers have three main classes.[3] The first category, named alkaline water electrolyzers (AWEs), is technologically mature and commercially available. In AWEs, the anode and cathode are immersed into an electrolyte solution containing about 6 M KOH, and the two compartments are divided by a porous diaphragm. This separation does not allow for pressurizing the hydrogen formed. The two electrodes need to be separated, increasing the ohmic resistance of the system and lowering the performance. AWEs, in fact, produce hydrogen at low current density in the order of 0.5 A cm^{-2}.[4–6] On the other hand, the second type is represented by proton exchange membrane water electrolyzers (PEMWEs). The electrodes in PEMWEs are separated by a polymeric proton exchange membrane, allowing the electrochemical pressurization of the hydrogen within the system itself. PEMWEs have the highest performance and are able to reach

a Department of Materials Science, University of Milano-Bicocca, U5, Via Cozzi 55, 20125, Milano, Italy. E-mail: carlo.santoro@unimib.it
b Istituto di Chimica Dei Composti OrganoMetallici (ICCOM), Consiglio Nazionale Delle Ricerche (CNR), Via Madonna Del Piano 10, 50019 Sesto Fiorentino, Firenze, Italy
c Istituto di Tecnologie Avanzate per l'Energia "Nicola Giordano" (ITAE), Consiglio Nazionale delle Ricerche (CNR), Via Salita S. Lucia sopra Contesse 5, Messina, 98126, Italy
d Department of Engineering, University of Palermo, Viale delle Scienze, 90128, Palermo, Italy
e Area Science Park, Elettra-Sincrotrone Trieste, Basovizza, Trieste, Italy
f Department of Physics, Computer Science and Mathematics, University of Modena and Reggio Emilia, Via Campi 103, 41125 Modena, Italy
† Electronic supplementary information (ESI) available. See DOI: https://doi.org/10.1039/d3im00058c

© 2023 The Author(s). Co-published by the Institute of Process Engineering, Chinese Academy of Sciences and the Royal Society of Chemistry

Ind. Chem. Mater., 2023, **1**, 343–359 | 343

Fig. 1 (a) TEM characterization of the Ni 600 °C and Ni 900 °C samples. For each sample, leftmost top image and bottom image report HRTEM characterization, while the rightmost column reports the STEM EDX mapping. (a) The Ni sample functionalized at 600 °C (Ni 600), and (b) the sample functionalized at 900 °C (Ni 900).

outcomes of the given research work contribute to the development of efficient electrocatalysts for HER to replace PGM-based electrocatalysts.

2 Results and discussion

2.1 Morphological investigation

The physicochemical characterizations of the as-developed electrocatalysts began through morphological and compositional investigations using multiple spectroscopic and microscopic techniques, such as high-resolution transmission electron microscopy (HRTEM), scanning transmission electron microscopy (STEM), and energy dispersive X-ray spectroscopy (EDX). From the characterization, some degree of nanoparticle formation was visible for all of the sample series (mono-, bi- and tri-metallic), both for 600 °C to 900 °C, with an important dimensional increase for the higher temperatures. Starting
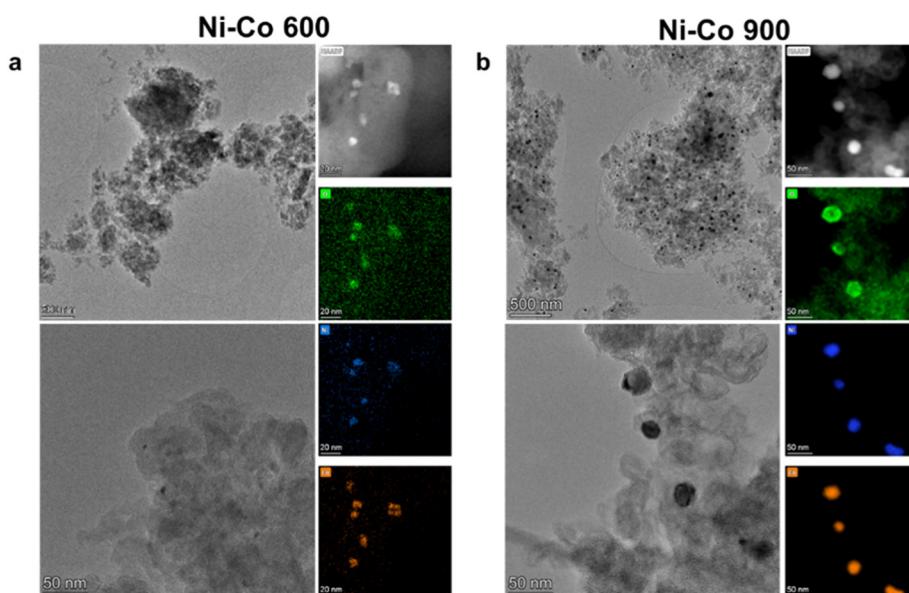
Fig. 2 (a) TEM characterization of the Ni–Co 600 °C and Ni–Co 900 °C samples. For each sample, leftmost top image and bottom image report HRTEM characterization, while the rightmost column reports the STEM EDX mapping. (a) The Ni–Co sample functionalized at 600 °C (Ni–Co 600), and (b) the sample functionalized at 900 °C (Ni–Co 900).

© 2023 The Author(s). Co-published by the Institute of Process Engineering, Chinese Academy of Sciences and the Royal Society of Chemistry

Ind. Chem. Mater., 2023, **1**, 343–359 | **345**
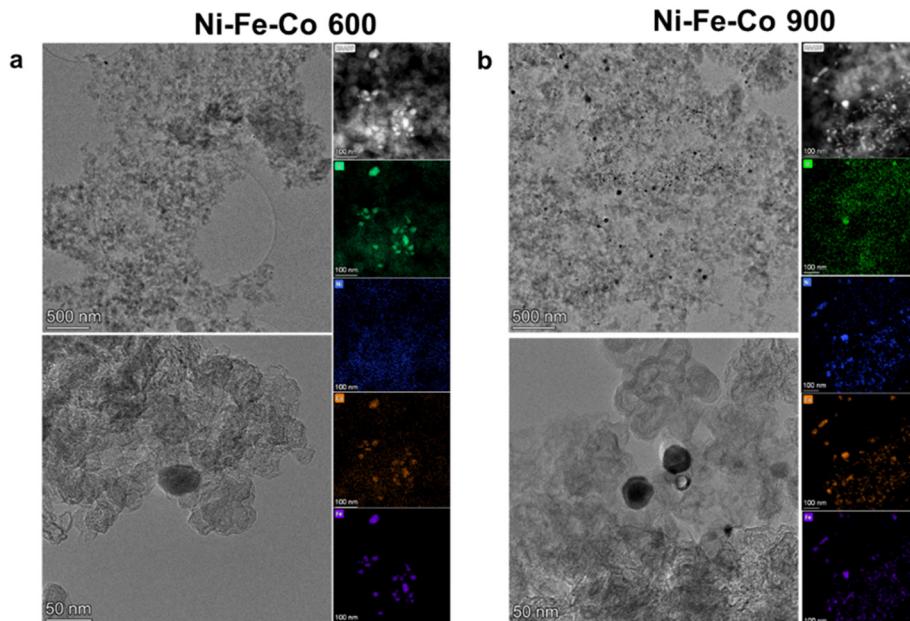
Fig. 3 (a) TEM characterization of the Ni–Fe–Co 600 °C and Ni–Fe–Co 900 °C samples. For each sample, leftmost top image and bottom image report HRTEM characterization, while the rightmost column reports the STEM EDX mapping. (a) The Ni–Fe–Co sample functionalized at 600 °C (Ni–Fe–Co 600), and (b) the sample functionalized at 900 °C (Ni–Fe–Co 900).

from the mono-metallic Ni samples, the comparison of the two process temperatures is shown in Fig. 1, where an increase of the dimension of the nanoparticles can be observed as the temperature increases, together with a change of shape. In Ni 600, the nanoparticles tend to have a cubic shape, with an average side dimension of 26 nm. Meanwhile, the nanoparticles modify their shape to spherical in Ni 900, with an average diameter of about 45 nm. This change is almost doubled with respect to the 600 °C ones. Regarding the compositional maps obtained by EDX by comparing the Ni and the O maps, a superimposition of the signal from the two elements can be observed in Ni 900. This observation reveals that the Ni nanoparticles in the former sample are mainly in the form of oxides. This is much more difficult for sample Ni 600, where no strong oxide signal can be correlated to the Ni presence in the nanoparticles, suggesting a very thin oxide layer on the surface.

The characterization results over Ni–Co 600 and Ni–Co 900 are reported in Fig. 2. From the HRTEM images, although spherical nanoparticles can be found in both electrocatalyst structures, there are more nanoparticles with larger sizes in Ni–Co 900 (average diameter 36 nm) compared to Ni–Co 600 (average diameter 5 nm). The HAADF results confirm this observation. Regarding the EDX results, it is possible to see that the visible particles in both samples are made of both Ni and Co, with an average atomic ratio of 1 : 2, and that they are mainly made by oxides. The presence of a strong background signal for nickel and cobalt in the 600 °C sample also suggests an incomplete conversion of the two elements in the nanoparticles.

Regarding the comparison between the Ni–Fe–Co 600 and Ni–Fe–Co 900 (tri metallic) electrocatalysts in Fig. 3, HRTEM

and HAADF demonstrate the existence of nanoparticles in the electrocatalyst structures for both temperature ranges. Qualitatively speaking, it is interesting to notice how the particles tend to maintain a smaller dimensional dispersion for the 600 °C sample (about 28 nm diameter), while an increase in the number of nanoparticles and a bigger dimensional spread (from 15 to 60 nm) can be seen in the 900 °C sample. Moreover, according to the EDX acquisitions, nanoparticles in Ni–Fe–Co 600 were composed mainly of Fe oxides (>90% at) with Ni as a lesser element (<2% at). Meanwhile, for the Ni–Fe–Co 900, the ratio between the elements seems to change, with an increase in the Co (approx. 50% at) and an intermediate amount of Fe (approx. 30% wt).

2.2 Raman analysis

In Fig. 4, the Raman spectra of the Ni-based electrocatalysts are shown. The Raman spectra were mainly composed of typical carbon signatures, where the G band located at ~1580 cm^{-1} is attributed to the E_{2g2} vibration mode of sp^2 bonded carbon atoms in graphite with D_{6h}^4 crystal symmetry, while the D band or the defect band emerges at ~1350 cm^{-1} due to in-plane defects and heteroatoms and imperfections in sp^2 carbon structures.[37–39] Two other peaks can also be recognized, especially in the spectra related to the functionalized electrocatalyst at 600 °C. The first one is the D_2 band (D*), which appears at ~1620 cm^{-1} as a shoulder on the G band.[40] The discontinuity defects offer the lost momentum needed to satisfy the resonant process in intravalley double resonance scattering, and it causes the emergence of the D* band.[41–44] This defect-induced Raman
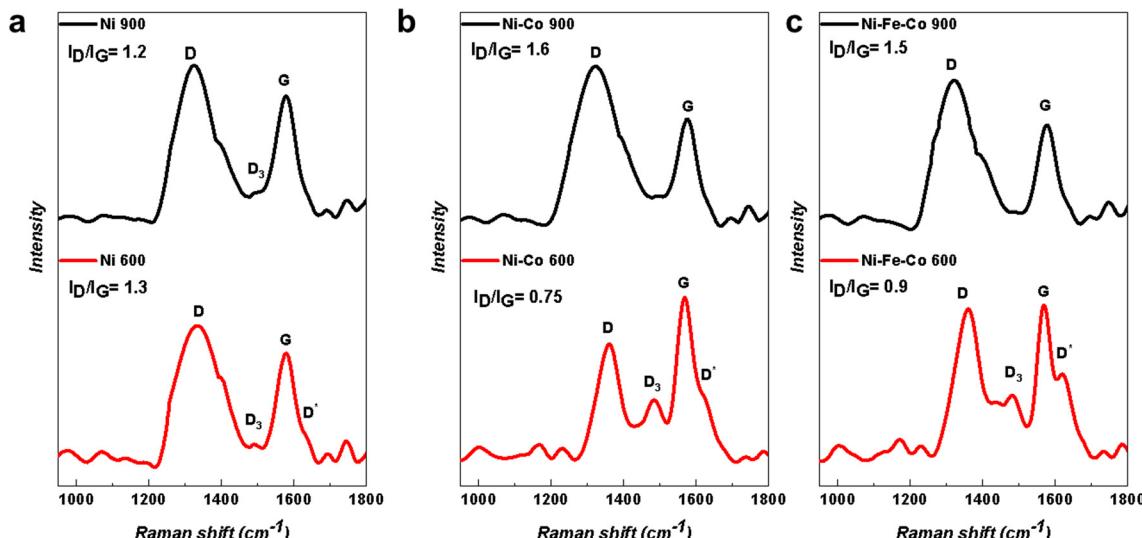
Fig. 4 Raman spectra of the Ni-based electrocatalysts with two different functionalization temperatures of 600 °C and 900 °C for the (a) Ni; (b) Ni–Co; and (c) Ni–Fe–Co samples.

feature usually shows up in very poorly organized carbon structures, and is absent in highly crystalline structures.[41,45–48] Another peak occurs only in poor crystallized carbon at ~1500 cm^{-1} and is called the D_3 band. Defects outside the plane of aromatic layers, such as tetrahedral carbons, are the reasons for the existence of D_3 band.[38,40] The integrated intensity ratio I_D/I_G for the D band and G band is used as quantitative parameters of the graphitization process and for characterizing the defect quantity in graphitic materials. Graphitization plays an important role the electron transfer during electrocatalysis. Besides graphitization, defects and discontinuities within the carbonaceous structure are considered electrocatalytically active moieties for HER.[49,50]

According to the Raman spectra in Fig. 4, the electrocatalysts with a functionalization temperature of 900 °C had a higher degree of graphitization compared to the samples with a functionalized temperature of 600 °C. In fact, by increasing the functionalization temperature, the intensity

ratio I_D/I_G was changed. In the case of the mono-atomic Ni-based electrocatalyst samples (Ni 600 and Ni 900) (Fig. 4a), the I_D/I_G ratio decreased. However, in the case of bi-metallic (Ni–Co 600 and Ni–Co 900) and tri-metallic (Ni–Fe–Co 600 and Ni–Fe–Co 900) (Fig. 4b and c), the situation is the opposite and an increase in the I_D/I_G ratio can be observed.

2.3 X-ray diffraction results and interpretation

XRD was used to study the crystallographic features of the as-developed electrocatalysts, as shown in Fig. 5. Two broad peaks centering at *ca.* 24° (002) and 44° (101) that belong to the amorphous carbon are visible.[51] These peaks came from the backbone carbon of the electrocatalyst that makes up the majority of the electrocatalyst itself. Except for the NiPc sample, the electrocatalysts functionalized at 600 °C showed two broad (002) and (101) carbon peaks (Fig. 5b and c) and no other peaks were detected. However, in the case of nickel, the XRD peaks related to metallic Ni showed up (Fig. 5a).
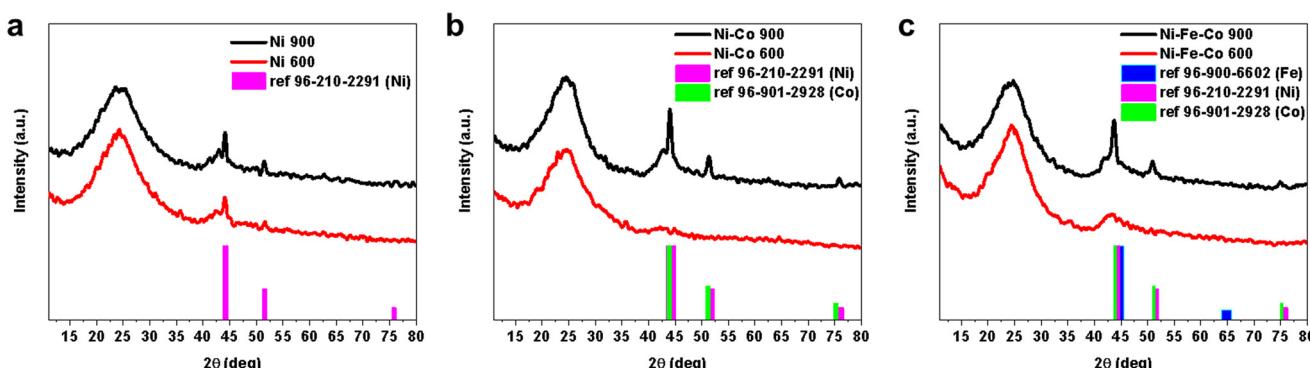

Fig. 5 XRD spectra of Ni-based electrocatalysts with two different functionalization temperatures of 900 °C and 600 °C for the (a) Ni; (b) Ni–Co; and (c) Ni–Fe–Co samples.

This is because the amount of NiPc in this sample (30 wt%) is higher than in other samples (15 wt% from each metal-Pc in bi-metallic and 10 wt% from each metal-Pc in tri-metallic). This partially contradicts the TEM images, where nanoparticles were detected. However, it is probable that these nanoparticles were present in such a small fraction that it was below the detection limit of the XRD instrument.

Meanwhile, in the XRD spectra related to the electrocatalyst with a functionalization temperature of 900 °C, sharper peaks belonging to the metallic species appeared (Fig. 5a–c). It is a sign of the existence of the metal cluster inside the as-synthesized electrocatalysts functionalized at 900 °C. The metallic nanoparticles appeared in these samples due to the fact that the metal atoms have enough mobility to shape the nanoparticles and small metallic clusters at 900 °C.[52,53] Even in the KJB Ni-based electrocatalysts, the intensity of the metallic Ni XRD peaks increased from Ni 600 °C to Ni 900 °C.

2.4 XPS analysis

The survey spectra shown in Fig. S1† reveal that no undesired elements are present on the surface of the six prepared samples. Atomic percentages, derived from the survey spectra, show that the electrocatalysts treated at higher temperatures have a relatively higher content of carbon (C1s) and a lower content of nitrogen (N1s). As detailed in Table S1,† the carbon amount ranges from 92.9% to 94.4% for the electrocatalysts treated at 600 °C, and it swings between 95.7% and 97.3% for the electrocatalysts treated at 900 °C. The major contribution in the nitrogen species is encountered for Ni–Fe–Co 600 (5.1%), whereas Ni–Co 900 and Ni 900 possess only 1.1%. This is probably due to the degradation and consequent evaporation of the nitrogen

species at a higher temperature. On the surface of each electrocatalyst, there is even a low atomic percentage of metal particles (<0.4%), such as iron, cobalt, or nickel.

Carbon, which accounts for over 90% of the overall electrocatalyst composition, is an extremely important component of the electrocatalysts studied in alkaline media. Nowadays, it is believed that the effect of graphitic, pyridinic, and pyrrolic nitrogen is negligible compared to the hydroxyl group over the electrocatalyst surface.[54] Moreover, the atomic percentage of nitrogen is very low in many samples, and this results in highly scattered signals in the XPS spectra. In an attempt to deconvolute the spectra (Fig. S2†), it seems that Ni–Fe–Co 600 and Ni–Co 600 exhibit the largest relative percentages of N-metal interactions, as described in Table S2,† whereas the signal is too weak to have an experimental value for the other electrocatalysts.

Deconvoluted C1s spectra of the six samples are highlighted in Fig. 6. Graphitic carbon at 284.4 eV, secondary carbons bonded to C–N or C–O at 285 eV, CN$_x$ defects at 286.2 eV, C–OH/C–OC at 287.1 eV, C=O at 288 eV and COOH at 289.4 eV were considered and fitted to obtain the relative percentages of each species, and are reported in the histogram of Fig. 7. Ni 900 is characterized by the lowest relative percentage of either graphitic carbon or C–N defects, whereas Ni–Co 900 showed the largest content of C–N defects and the second higher percentage of graphitic carbon (62.1%) among the investigated KJB-supported compounds. By comparing the Ni–Fe–Co catalysts, treated at 600 °C or 900 °C, the relative percentages of graphitic and C–N defects are slightly larger for Ni–Fe–Co 600. In contrast, the secondary carbons bonded to nitrogen or oxygen are lower than that obtained for Ni–Fe–Co 900. Furthermore, it is necessary to highlight that the atomic percentage of nitrogen
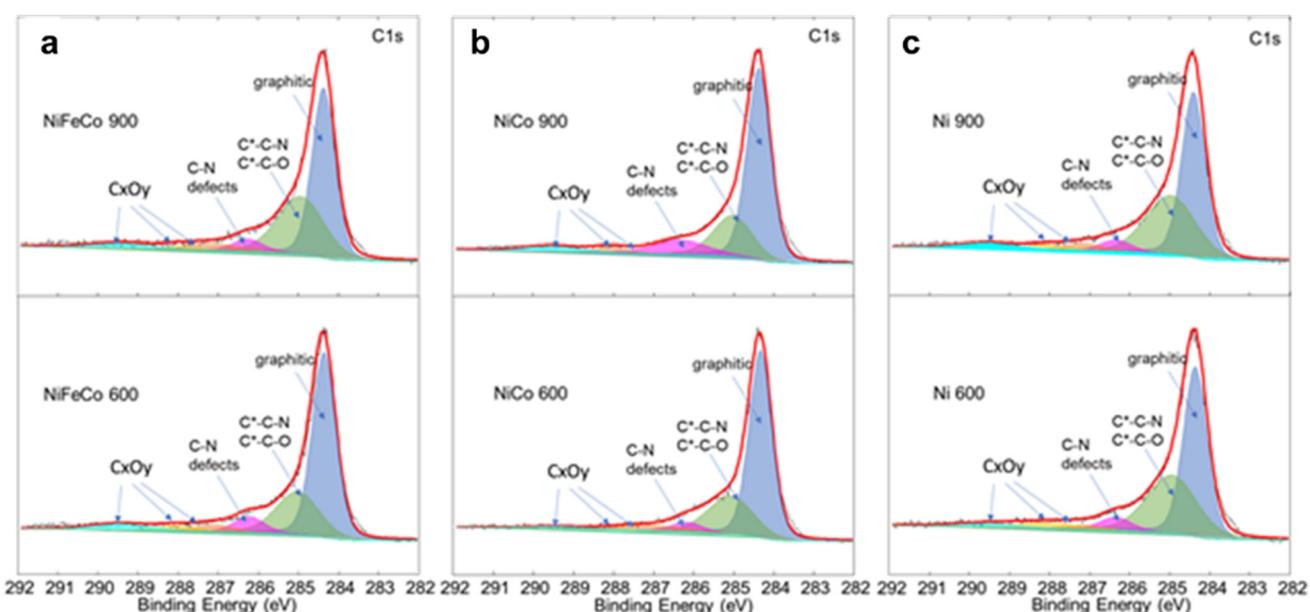
Fig. 6 Comparison of the XPS C1s signal for (a) Ni–Fe–Co 600 and Ni–Fe–Co 900, (b) Ni–Co 600 and Ni–Co 900, and c) Ni 600 and Ni 900.
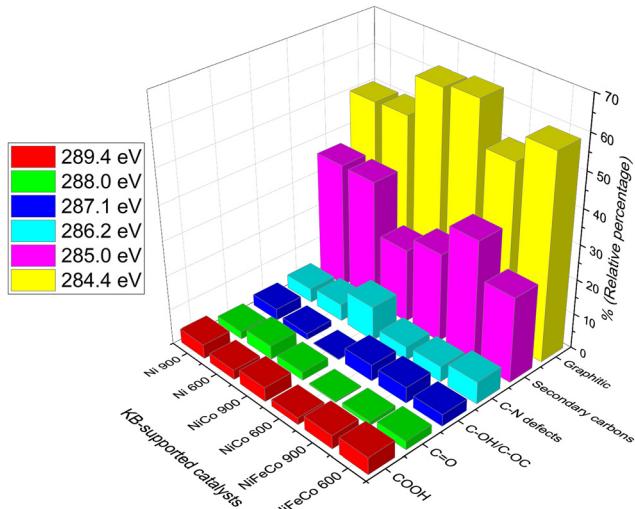
Fig. 7 Histogram of the relative percentages of C1s species for the Ni-based KJB-supported electrocatalysts collected by the integration of the deconvoluted peaks provided in Fig. 6.

for Ni–Fe–Co 900 (5.1%) is about three times that of Ni–Fe–Co 600 (1.8%).

2.5 XAS results and analysis

Ex situ XAS analysis of the electrocatalysts Ni, Ni–Co and Ni–Fe–Co pyrolyzed at 600 °C and 900 °C was carried out. XAS measurements were performed to study the oxidation, folding and evolution of the chemical environment of the singular and alloyed TMs (Fe, Co, or Ni). XANES and EXAFS spectra were analyzed using the Athena software (Demeter package).[55] The data were acquired around the K absorption edge for Ni in the energy range centered at the edge nominal value (namely $E_0(\text{Ni}) = 8333$ eV), in a range that spans the energies from $(E_0 - 300)$ to $(E_0 + 1000$ eV). For Fe and Co, the ranges are limited to $E_0 + 600$ eV due to the interference of the borders of Co and Ni ($E_0(\text{Fe}) = 7112$ eV and $E_0(\text{Co}) = 7709$ eV). The XANES data were normalized at $E–E_0$. In this way, the same features were observed in the same energetic value (Fig. 8). On the top axis, the features common to phthalocyanine samples were marked, as reported by Rossi *et al.*[56]

Fig. 8a and b show the spectra of the samples collected at room temperature and after being heated at 600 °C. All of the XANES spectra except for those referring to the Fe K-edge (red) show the features of the phthalocyanine molecules, in

Fig. 8 Plots on the left (a–c): normalized XANES spectra of the transition metals in the range $E–E_0 \in [-10–100]$ eV, where E_0 is the K edge. The spectra are grouped by element, each one with a corresponding color: green for Ni, yellow for Co, and red for Fe. The shape of the line is representative of the sample: solid for the Ni monometallic, dot-dash for the Ni–Co bimetallic sample, and, dashed line for the Ni–Fe–Co trimetallic electrocatalysts. (a) the spectra collected on the samples at room temperature. (b) The ones collected after heating the samples at 600 °C. (c) The spectra collected after pyrolysis at 900 °C. plots on the right (d-f): FT EXAFS-plots (R) of the transition metals, phase-corrected; (d) spectra collected at room temperature; (e) after heating treatment at 600 °C; and (f) after pyrolysis at 900 °C.

particular the peak A_2, assigned to the 1s to 4p transition and the pre-edge peak, A_1, which is assigned to the 1s to 3d dipole forbidden (quadrupole) transition, better shown in the subplots on the bottom-right.[56,57]

The Fe spectra, on the contrary, did not show the A_2 peak. The pre-edge was shifted from 0 to 3 eV, and the other features also appeared less resolved (see the B_2, D and E bands). The pre-edge peaks observed on the iron spectra had the same energy observed in other iron oxides (α- and γ-Fe_2O_3 and Fe_3O_4) (Fig. S3†). Instead, in the heated sample (600 °C and 900 °C), the Fe spectrum showed the 1s to 4p transition peak, although with very low intensity with respect to the other transition metals. The different XANES spectra for iron suggested a different geometry, with the symmetry changing from D_{4h} to C_{4v}, and the change of the structure from planar to square pyramidal with the bonding of an oxygen atom.[58]

The XANES spectra collected on the pyrolyzed samples show a change in the profiles, reflecting a change in the structure around the transition metals. Fig. 8d–f show the EXAFS spectra in the R space, wherein the top x-axis displays the assignments of the different peaks considering the possible environments (phthalocyanine and metallic).[56,59–61] Fig. 8d and e show the features related to the phthalocyanine molecule: TM–N_{iso}, TM–C_α, TM–N_{aza}, and TM–C_γ bonds. Fig. 8f shows the formation of metallic bonds (TM–TM) during thermal treatment with the appearance of a new peak at around 2.4 Å. It can be inferred then that metal nanoparticles are formed at a temperature between 600 °C and 900 °C.

Linear combination fitting (LCF) analysis of the XANES spectra of the pyrolyzed samples at 900 °C (Fig. S4†) also shows the formation of metallic bonds. Indeed, the measured spectra could be reproduced by combining the spectrum collected on the Ni-based electrocatalysts heated at 600 °C

with the metal spectrum. For Co, an acceptable fit cannot be obtained without using CoO, suggesting that Co is also present in this form (Table S3†).

XANES spectra do not allow us to distinguish between the TM–N_2, TM–N_3, and TM–N_4 bonds. This would be theoretically possible with FT-EXAFS refinements, but the presence of different kinds of foldings in the samples makes it really difficult to reliably perform the fitting of the EXAFS spectra. However, in the pyrolyzed Ni and Fe, the LCFs show that new metal bondings are created in all of the systems analyzed, while Co is the only metal to be also oxidized. The fitted percentages for the metallic component are nearly the same for all of the samples (between 40% and 47%) with the exception of Co in the Ni–Co samples, for which the metallic component seems to be higher. Regarding the Pc component, we observe nearly the same percentage (around 53–60%) for Fe and Ni, but a much lower value for Co, as the oxide also is formed. This fact suggests that in any case, cobalt seems to be more prone to react, even though it is converted both in its metallic and oxide forms.

2.6 Electrochemical measurements

2.6.1 Effect of the Ni phthalocyanine precursor weight percentage on the HER electrochemical performance. The electrochemical measurements over the KJB Ni-based electrocatalyst were performed and analyzed for HER. To determine the electrochemical performance of the samples in alkaline media, linear sweep voltammetry (LSV) was run with the conditions described in the experimental section and the obtained results are shown in Fig. 9. Based on the literature, overpotentials were calculated at a current density of −10 mA cm^{-2} and are reported in Table 1.[3]

Initially, the NiPc used as a precursor for the synthesis of the Ni-based HER electrocatalyst varied between 10 wt% and
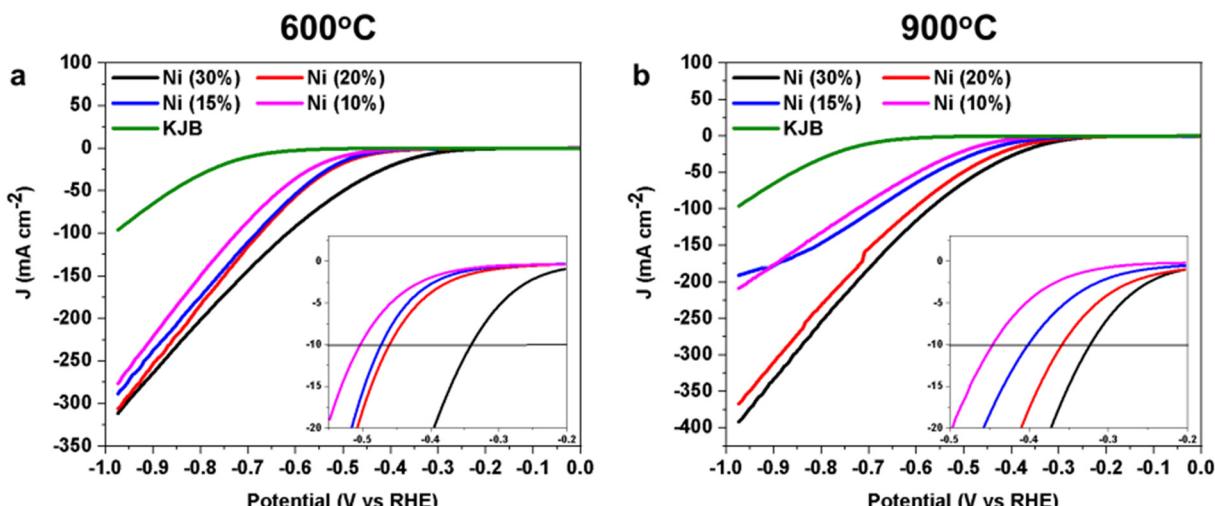

Fig. 9 The LSVs of the RDE measurement of KJB Ni-based electrocatalysts with different wt% of NiPc in their composition, and different thermal treatment temperatures of (a) 600 °C and (b) 900 °C in N_2 saturated KOH (1 M) solution. The scan rate of 5 mV s^{-1} and a rotating disk speed of 1600 rpm were used for the measurements. The KJB carbon was measured as a control.

Table 1 The HER overpotential belonging to the KJB Ni-based electrocatalysts with different wt% of NiPc in their composition and different thermal treatment temperatures

Sample	Overpotential (V)
Ni (30%) 900	0.32
Ni (30%) 600	0.34
Ni (20%) 900	0.35
Ni (20%) 600	0.46
Ni (15%) 900	0.40
Ni (15%) 600	0.47
Ni (10%) 900	0.44
Ni (10%) 600	0.50

30 wt%. These tests were carried out in order to establish correlations between the metal content and performance. HER performances of the Ni electrocatalysts with different weight percentages (wt%) of NiPc were examined (Fig. 9). In the obtained result, the relationship between the wt% of the NiPc in the electrocatalysts and their HER performance were reported. Ni (30%) 900, which has the highest amount of NiPc wt%, showed the best performance with an overpotential of 0.32 ± 0.01 V (at −10 mA cm^{-2}). By decreasing the amount of NiPc in samples, the overpotential increased. It was found that by increasing the NiPc wt%, the HER active sites increase too. This was mainly based on the metallic nanoparticles, as confirmed through the microscopic and spectroscopic investigations (Table 3). Meanwhile, the effects of different thermal treatment temperatures on the HER activity performance are significant. The electrocatalysts pyrolyzed at 900 °C showed much lower overpotential in comparison to the same electrocatalyst, but with a lower pyrolysis temperature (600 °C). According to the reported results in the other characterization sections, the electrocatalysts with 900 °C pyrolysis temperature possess a greater number of Ni nanoparticles, which play an important role as active sites for HER.[62]

The stability test on Ni 900 (30 wt% of NiPc) is shown in Fig. 10. At 10 mA cm^{-2}, the measured overpotential changed significantly within the first 500 cycles (it dropped from −0.32 ± 0.01 V to −0.36 ± 0.01 V). Between the 500th and 2500th cycles, the HER electrocatalytic activity remained stable. This electrocatalyst has shown considerable durability in 1 M KOH solution.

Table 2 The HER overpotential of the Ni-based electrocatalysts with different compositions of materials and different thermal treatment temperatures

Samples	Overpotential (V)
Ni 900	0.32
Ni–Fe–Co 900	0.32
Ni–Fe–Co 600	0.32
Ni 600	0.34
Ni–Co 900	0.34
Ni–Co 600	0.34

In agreement with the existing literature, the increase of Ni loading in the electrocatalyst, from 10 wt% to 30 wt%, improved the HER electrocatalytic activity.[63–66] By increasing the Ni loading, the number of active sites in the electrocatalyst increased, leading to the enhancement of the Ni-based electrocatalytic activity.[67] In addition, the effect of different functionalization temperatures on the electrocatalyst with different NiPc was demonstrated. The HER performance due to the functionalization at two different temperatures of 600 °C and 900 °C is not much in the electrocatalyst with 30 wt% (0.02 mV different in overpotential). However, the difference in the overpotential suddenly increased when the NiPc wt% decreased.

2.6.2 Effect of Ni alloying on the HER electrochemical performance. To evaluate the Ni-based electrocatalysts that possess 30 wt% of different combinations of transition metals-phthalocyanine in a mono-, bi-, and tri-metallic fashion, the HER performance was used with the same RDE method explained in the last section. As Fig. 11 shows, in the mono-metallic NiPc-included samples, the Ni 900 with an over-potential of 0.32 ± 0.01 V performed better than the Ni 600 sample with an overpotential of 0.34 ± 0.01 V. This is due to the formation of larger Ni metal nanoparticles at 900 °C that favor HER.[62] Meanwhile, in the bi-metallic Ni–Co (Ni–Co 600 and Ni–Co 900) and tri-metallic (Ni–Fe–Co 600 and Ni–Fe–Co 900) samples, there is no difference between the two different functionalization temperatures from the overpotential point of view. In the Ni–Co and Ni–Fe–Co electrocatalysts, the thermal treatment not only had an effect on the size and number of alloy nanoparticles, but also had some effect on the type of alloys. For example, the Ni–Fe–Co EDX maps have shown the existence of Fe–Co oxide in Ni–Fe–Co 600. Meanwhile, in Ni–Fe–Co 900, the transition metals formed the Ni–Fe–Co alloy. Both tri-metallic Ni–Fe–Co electrocatalysts have the best performance (besides the Ni 900) with an overpotential of 0.32 ± 0.01 V (Table 2).

The stability tests over the Ni–Co 900 and Ni–Fe–Co 900 electrocatalysts are shown in Fig. S5.† For these samples, similar to Ni 900, a performance reduction in the first 500 cycles was also observed. However, their overpotentials remained stable between the 500th and 2500th cycles, which indicates their stability in 1 M KOH solution.

For the sake of comparison, stability tests were also performed for 30 wt%. NiPc/KJB without pyrolysis treatment (Fig. S6†). However, when comparing the stability tests of the Ni samples with and without thermal treatment, valuable insights were gained regarding the positioning of the Pc rings within the electrocatalyst. The Ni 900 sample exhibited notable stability, whereas the Ni (30%) sample without thermal treatment (Fig. S6†) displayed very poor stability (less than 150 cycles). This instability might be due to the fact that the Pc rings remained on the surface of the underlying carbon structure, and were not embedded into the carbon skeleton.[77]

© 2023 The Author(s). Co-published by the Institute of Process Engineering, Chinese Academy of Sciences and the Royal Society of Chemistry

Ind. Chem. Mater., 2023, **1**, 343–359 | **351**

Table 3 The electrocatalysts studied and the synthesis steps performed for different wt% values of NiPc

| Sample	Mix with metal-Pc	Functionalization	
	Ni Pc	600 °C	900 °C
Ni (30%) 600	30 wt%	■	
Ni (30%) 900	30 wt%		■
Ni (20%) 600	20 wt%	■	
Ni (20%) 900	20 wt%		■
Ni (15%) 600	15 wt%	■	
Ni (15%) 900	15 wt%		■
Ni (10%) 600	10 wt%	■	
Ni (10%) 900	10 wt%		■

2.7 Outlook and perspectives

Bimetallic and trimetallic nitrogen-doped carbon electrocatalysts have also been studied and presented in the literature. For bimetallic electrocatalysts, Lihua Hu *et al.* worked on a high-density nickel–cobalt alloy embedded in nitrogen-doped carbon nanosheets. Zhang *et al.* also reported on the Fe–Ni bimetallic N-doped carbon framework performance for HER.[68,69] Compared to these related works, with respect to the loading of NiPc and CoPc in Ni–Co electrocatalysts, the HER performances of Ni–Co 600 and Ni–Co 900 are acceptable. The effect of thermal treatment was also shown, which allowed for the formation of metallic alloy nanoparticles at high temperatures. Despite their high potential, trimetallic electrocatalysts have not received much attention and only a few studies were presented. In this way, Yuling Xu *et al.* worked on the Fe/Co/Ni alloy electrode. Ziqi Zhang *et al.* also demonstrated the real potential of trimetallic electrocatalysts, reporting their work on FeNiMo trimetallic nanoparticles encapsulated in carbon cages.[32,70]

Fig. 10 HER stability test (2500 cycles) on the Ni 900 electrocatalyst.

However, Mo is not stable in alkaline conditions. A comparison between the obtained results and the literature is presented in Table S4 (ref. 50 and 68–76).†

Many lessons were learned from the current work. Ni-based electrocatalysts were shown to be promising for HER. Nickel being the 10th group, shares a similar electronic configuration compared to Pd and Pt. Despite starting from a single atom precursor (*e.g.*, phthalocyanine), at both 600 °C and 900 °C pyrolysis temperature, nanoparticles of different nanometric scales are present. At room temperature (no heat treatment) and 600 °C, the majority of the active sites is in the TM–N_x configuration and this is confirmed by the FT EXAFS plots. Unfortunately, XPS could not be used to quantitatively identify the metal percentage, as it was below the detection limit. Importantly, through XPS, it was possible to identify the TM–N_x relative percentage by deconvoluting the N1s spectra. Higher temperature led to the formation of a greater number of metallic nanoparticles that are beneficial for HER. This was confirmed by both TEM and EXAFS, as well as XRD.

For Ni-based monometallic electrocatalysts, higher nickel-containing precursors are also beneficial in improving the electrocatalytic activity. Future studies might further increase the amount of NiPc within the precursor. The higher electrocatalytic activity achieved with Ni 900 highlights that Ni nanoparticles, rather than Ni–N_x (atomically dispersed active site), are more efficient for HER. At 600 °C, a lower of nanoparticles with lower dimensions were also identified. However, Ni–N_x active sites were prevalent. Importantly, the low durability of the NiPc–KJB electrocatalyst without undergoing thermal treatment highlights the fact that the Pc is not embedded in the carbonaceous backbone.

Interestingly, the addition of the second metal (Co) and the third metal (Fe) has an effect on surface chemistry and electrocatalytic activity. In general, the addition of more metals within the electrocatalyst creates a more difficult situation to explain since a greater multitude of active sites are present. In fact, the TM(s)Pc exist and are embedded in
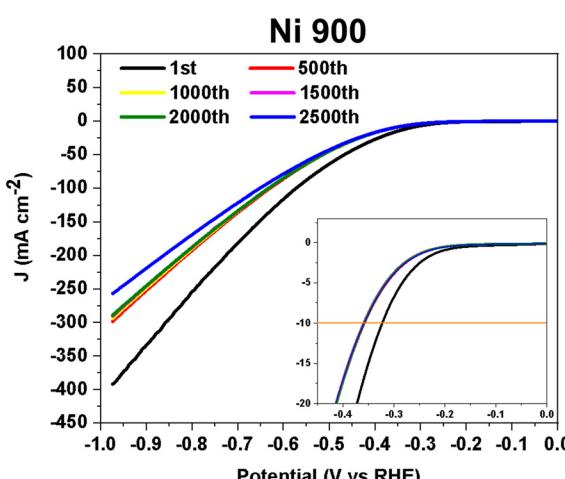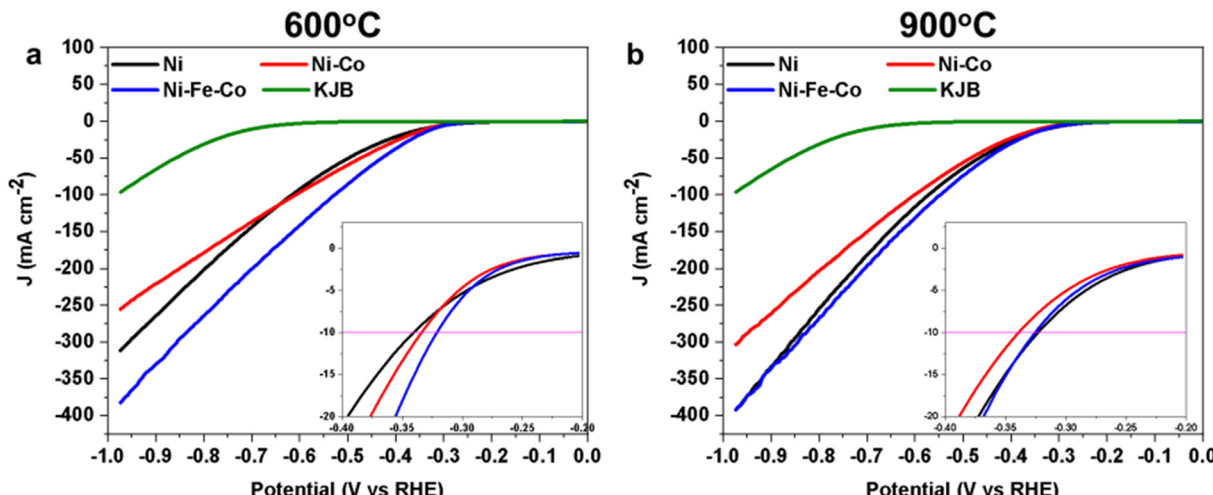
Fig. 11 The LSVs of RDE measurement for the KJB Ni-based electrocatalysts with different compositions of materials and different thermal treatment temperatures of (a) 600 °C and (b) 900 °C in N_2 saturated KOH (1 M) solution. The scan rate of 5 mV s^{-1} and a rotating disk speed of 1600 rpm were used for the measurements. The KJB carbon was measured as a control.

the carbon structure. The nanoparticles are formed already at 600 °C and the alloys are created. FT EXAFS plots highlight the formation of nanoparticles at higher temperature. The trimetallic electrocatalyst showed similar electrocatalytic activity after the pyrolysis at 600 °C and 900 °C, and similar results were obtained compared to Ni 900. However, in bimetallic and trimetallic configurations, the weight percentage of the TM(s) was maintained at 30%. Therefore, in the trimetallic configurations, the weight percentage of Ni was only 10 wt%. Further study will focus on increasing the weight percentage of the TM(s) to enhance the quantity of TM(s) over the carbon support, which in this study, was lower than 2 wt%. We can speculate that the formation of nanoparticles (alloys and oxides) and the co-presence of multiple single active centers are beneficial for HER, acting synergistically. In this case, it is quite complicated to discriminate among the reactivity of each single active site, as a multitude of active sites are present.

All of the relevant morphological and analytical observations for Ni-based electrocatalysts are summarized in Table S5.†

3 Conclusion

The mono-/bi-/tri-metallic Ni-based electrocatalysts were synthesized by mixing the required TM–Pc with a conductive carbon backbone, and then applying the thermal treatment in a controlled atmosphere and temperature. The electrocatalysts, functionalized at two different temperatures (600 °C and 900 °C), were characterized and tested for HER. The results showed that the increase in Ni–Pc wt% in the initial mixture (from 10 wt% to 30 wt%), enhanced the HER activity. The effect of different pyrolysis temperatures on electrocatalysts was studied by XAS and HR-TEM characterization techniques, demonstrating the formation of nanoparticles, especially at higher temperatures (larger

number and size). In the comparison between the two functionalized temperatures, the samples functionalized at 900 °C had a greater number of nanoparticles with larger sizes. Ni 900 (containing 30 wt% of NiPc as the initial precursor) demonstrated higher electrocatalytic activity as a monometallic electrocatalyst with an overpotential of 0.32 ± 0.01 V (at −10 mA cm^{-2}). Excellent durability was also demonstrated in alkaline media using accelerated stress tests. It is also evident that adding a second (Co) and third (Fe) metal has a positive impact on the HER electrocatalytic activity.

4 Experimental section

4.1 Materials

KJB was purchased from Nanografi Nano Technology (Turkey), and it was used as the carbon backbone for the HER electrocatalyst. Potassium hydroxide (KOH), acetone ($(CH_3)_2CO$), and Nafion® 5 wt% hydro-alcoholic solutions were purchased from Sigma-Aldrich. Nickel(II) phthalocyanine ($C_{32}H_{16}N_8Ni$, named NiPc), iron(II) phthalocyanine ($C_{32}H_{16}N_8Fe$, named FePc,), and cobalt(II) phthalocyanine ($C_{32}H_{16}CoN_8$, named CoPc) were purchased from Acros Organics. Argon (Ar) and nitrogen (N) gases used in this study possess ultra-high purity. Ultrapure deionized water obtained from a Millipore Milli-Q system (resistivity >18 MΩ cm) was used for the experiments.

4.2 Electrocatalyst synthesis

A high-energy ball miller (E_{max} Retsch) was used to homogeneously mix the KJB carbon with different amounts of NiPc (10, 15, 20, and 30 wt%) using a rotation rate of 400 rpm for 20 min. Then, the functionalization thermal treatment was applied over the mixed samples with two different temperatures of 900 °C and 600 °C, separately, in the controlled Ar atmosphere (UHP Ar at 100 cm^3 min^{-1}).

According to the previous paper, the heating rate for increasing and decreasing the temperature was 5 °C min^{-1} before and after the dwell time, respectively.[78] The synthesized samples are reported in Table 3.

With the same approach, the TMs of choice (FePc, NiPc, and CoPc) were mixed with carbon, and functionalized with thermal treatment at two different temperatures of 600 °C and 900 °C (Table 4).

4.3 Characterization

4.3.1 TEM. A ThermoFisher Talos F200X G2 was used for high-resolution transmission electron microscopy (HRTEM) imaging with an acceleration voltage of 200 kV and a resolution of 4096 × 4096 pixels without any objective apertures. An annular STEM detector with a convergent beam angled at 10.5 mrad was used for the high-angle annular dark-field (HAADF) images. Super X spectrometers equipped with silicon drift detectors of 30 mm^2 were used to collect energy dispersive X-ray analysis (EDX) maps with a collection angle of 0.7 srad.

4.3.2 Raman spectroscopy. In this work, a Jasco Ventuno μ-Raman system that possesses a He–Ne laser (wavelength 632.8 nm, power density 6 kW cm^{-2}) was used. This device is equipped with a Peltier-cooled charge-coupled device (CCD) camera that has a −50 °C operating temperature. A single crystal Si sample, whose domain peak is at 520.65 cm^{-1}, was used as a reference sample for calibration.

4.3.3 X-ray diffraction. The copper source X-ray diffraction (XRD, Rigaku Miniflex 600) performed measurements with an angle range of 10–90° with a step of 0.020° and a scanning speed of 1.000° min^{-1} over powder samples.

4.3.4 XPS. The survey spectra and the deconvolution of the C1s species were carried out by X-ray photoelectron spectroscopy (XPS), Physical Electronics (PHI) 5800-01 using a monochromatic Al Kα X-ray source at a power of 350 W, as previously reported.[79,80] XPS data were processed with the help of recent results reported in the literature.[54,81–88]

4.3.5 XAS. X-ray absorption spectroscopy (XAS) spectra at the K-edges of Fe, Co and Ni were collected using a Si (111) monochromator and ionization chambers at the XAS beamline (ELETTRA, Trieste, Italy).[89] The collected spectrum from a metal foil placed in a second experimental chamber after the sample and after the I$_1$ ionization chamber was used as a reference for energy calibration. The first inflection point was taken at 7112, 7709 and 8333 eV for Fe, Co and Ni, respectively.

Each spectrum was collected at room temperature with a variable energy step: a large step (5 eV) in the first 200 eV, a smaller step (0.2 eV) in the X-ray absorption near-edge structure (XANES) region, and a k-constant step of 0.03 Å^{-1} in the extended X-ray absorption fine-structure (EXAFS) region. The measurements for each sample were run with 3 accumulations to increase the signal-to-noise ratio. Athena software was used to normalize the XANES spectra of the samples and model compounds to the atomic background.[55]

The normalized XANES spectra were then analyzed through linear combination fitting (LCF) of spectra from model compounds (available from the beamline database), using the Athena software.

4.4 Hydrogen evolution reaction (HER)

In this work, the three-electrode technique with the rotating disk electrode (RDE) was applied to measure HER. A glassy carbon (GC) disk with a geometric area of 0.1963 cm^2 was mounted on RDE equipment (Pine WaveVortex RDE system coupled with a Pine bipotentiostat) and used as a working electrode. For this experiment, an electrode rotation speed of 1600 rpm was maintained during the HER measurements. A saturated calomel electrode (SCE) and a Pt wire were used as a reference electrode and the counter electrode, respectively.

For testing the electrochemical properties of Ni-based electrocatalysts in powder form, proper inks were required. The inks were prepared by mixing (5 mg) of electrocatalyst powder with 15 μL of 5 wt% Nafion® D-520 ionomer solution and 985 μL of isopropanol with sonication, as suggested in previous reports. The 0.6 mg cm^{-2} loading of the mentioned inks was achieved by depositing over a GC disk.[90,91] Electrochemical measurements were performed in alkaline media (1 M KOH). Nitrogen gas was flushed into the alkaline solution from 25 min before starting the measurements to

Table 4 Ni-based electrocatalysts that were studied and the synthesis steps performed for different combinations of TM–Pc

Sample	Mix with metal-Pc			Functionalization	
	Fe Pc	Ni Pc	Co Pc	600 °C	900 °C
Ni 600		30 wt%		■	
Ni 900		30 wt%			■
Ni–Co 600		15 wt%	15 wt%	■	
Ni–Co 900		15 wt%	15 wt%		■
Ni–Fe–Co 600	10 wt%	10 wt%	10 wt%	■	
Ni–Fe–Co 900	10 wt%	10 wt%	10 wt%		■

Industrial Chemistry & Materials

remove residual oxygen from the electrolyte solution and prevent unwanted reactivity. The measured potentials were converted into potential *versus* reversible hydrogen electrode (RHE) using the following equation:[92]

$$E_{RHE} = E_{ref} + 0.059 \cdot pH + E_{ref}^0$$

E_{ref}^0 is the potential of the reference electrode with respect to the standard hydrogen electrode at 25 °C (0.241 V for SCE), and E_{ref} is the measured working potential *versus* the reference electrode. The potential window for all measurements was kept between 0 and −0.97 V *vs.* RHE, and the scan rate of 5 mV s^{-1} was used to record the polarization curves of the various developed electrocatalysts. The overpotential of each electrocatalyst was evaluated at the current density of −10 mA cm^{-2}.[93,94] The durability test of the Ni-based electrocatalyst was performed by using an accelerated stability test.[90,94] This measurement involved 2500 cycles at 50 mV s^{-1} with the potential range between 0 and −0.97 V *vs.* RHE. A polarization curve was measured at the first cycle and after every 500 cycles at a scan rate of 5 mV s^{-1}.

Author contributions

Conceptualization: SAM, MM, AL, CS. Data curation: SAM, MM, JO, EB, LC, AL, CLV, AZ, AG, FDF. Formal Analysis: SAM, MM, JO, EB, LC, AL, CLV, AZ. Funding acquisition: VB, AL, CS. Investigation: SAM, MM, EB, AL, CLV, AZ, LO, SP, CS. Methodology: AL, CS. Project administration: CS. Resources: SAM, JO, CLV, EB, LC, AL, AZ, FDF, MS. Supervision: LO, SP, MS, VB, AL, CS. Visualization: SAM, MM, CLV, EB, LC, AL. Writing – original draft: SAM, MM, JO, LC, AL, CLV, VB, AZ, FDF, SP, CS. Writing – review & editing: SAM, MM, JO, EB, SP, CS.

Conflicts of interest

There are no conflicts to declare.

Acknowledgements

References

1 A. Kusoglu, Chalkboard 1-the many colors of hydrogen, *Electrochem. Soc. Interface*, 2021, **30**, 44.

2 E. Commission, *Hydrogen*, **https://energy.ec.europa.eu/ topics/energy-systems-integration/hydrogen_en**, (accessed 7 July 2023).

3 C. Santoro, A. Lavacchi, P. Mustarelli, V. Di Noto, L. Elbaz, D. R. Dekel and F. Jaouen, What is next in anion-exchange membrane water electrolyzers? Bottlenecks, benefits, and future, *ChemSusChem*, 2022, **15**, e202200027.

4 M. David, C. Ocampo-Martínez and R. Sánchez-Peña, Advances in alkaline water electrolyzers: A review, *J. Energy Storage*, 2019, **23**, 392–403.

5 M. Rashid, M. K. Al Mesfer, H. Naseem and M. Danish, Hydrogen production by water electrolysis: a review of alkaline water electrolysis, PEM water electrolysis and high temperature water electrolysis, *International Journal of Engineering and Advanced Technology*, 2015, **4**, 2949–8958.

6 M. Schalenbach, A. R. Zeradjanin, O. Kasian, S. Cherevko and K. J. Mayrhofer, A perspective on low-temperature water electrolysis–challenges in alkaline and acidic technology, *Int. J. Electrochem. Sci.*, 2018, **13**, 1173–1226.

7 M. Carmo, D. L. Fritz, J. Mergel and D. Stolten, A comprehensive review on PEM water electrolysis, *Int. J. Hydrogen Energy*, 2013, **38**, 4901–4934.

8 S. Mukerjee, Y. Yan and H. Xu, Hydrogen at scale using low-temperature anion exchange membrane electrolyzers, *Electrochem. Soc. Interface*, 2021, **30**, 73.

9 Q. Li and S. Sun, Recent advances in the organic solution phase synthesis of metal nanoparticles and their electrocatalysis for energy conversion reactions, *Nano Energy*, 2016, **29**, 178–197.

10 F. Safizadeh, E. Ghali and G. Houlachi, Electrocatalysis developments for hydrogen evolution reaction in alkaline solutions–a review, *Int. J. Hydrogen Energy*, 2015, **40**, 256–274.

11 E. Commission, *Critical raw material*, https://single-market-economy.ec.europa.eu/sectors/raw-materials/areas-specific-interest/critical-raw-materials_en, (accessed 7 July 2023).

12 X. Zou and Y. Zhang, Noble metal-free hydrogen evolution catalysts for water splitting, *Chem. Soc. Rev.*, 2015, **44**, 5148–5180.

13 S. Sultan, J. N. Tiwari, A. N. Singh, S. Zhumagali, M. Ha, C. W. Myung, P. Thangavel and K. S. Kim, Single atoms and clusters based nanomaterials for hydrogen evolution, oxygen evolution reactions, and full water splitting, *Adv. Energy Mater.*, 2019, **9**, 1900624.

14 Q. Zhang and J. Guan, Atomically dispersed catalysts for hydrogen/oxygen evolution reactions and overall water splitting, *J. Power Sources*, 2020, **471**, 228446.

15 M. Ďurovič, J. Hnát and K. Bouzek, Electrocatalysts for the hydrogen evolution reaction in alkaline and neutral media. A comparative review, *J. Power Sources*, 2021, **493**, 229708.

16 F. Ullah, K. Ayub and T. Mahmood, High performance SACs for HER process using late first-row transition metals

© 2023 The Author(s). Co-published by the Institute of Process Engineering, Chinese Academy of Sciences and the Royal Society of Chemistry

Ind. Chem. Mater., 2023, **1**, 343–359 | 355

anchored on graphyne support: A DFT insight, *Int. J. Hydrogen Energy*, 2021, **46**, 37814–37823.

17 A. Baghban, S. Habibzadeh and F. Zokaee Ashtiani, On the evaluation of hydrogen evolution reaction performance of metal-nitrogen-doped carbon electrocatalysts using machine learning technique, *Sci. Rep.*, 2021, **11**, 21911.

18 Y. Meng, X. Huang, H. Lin, P. Zhang, Q. Gao and W. Li, Carbon-based nanomaterials as sustainable noble-metal-free electrocatalysts, *Front. Chem.*, 2019, **7**, 759.

19 L. Du, Y. Shao, J. Sun, G. Yin, J. Liu and Y. Wang, Advanced catalyst supports for PEM fuel cell cathodes, *Nano Energy*, 2016, **29**, 314–322.

20 L. Du, G. Zhang, X. Liu, A. Hassanpour, M. Dubois, A. C. Tavares and S. Sun, Biomass-derived nonprecious metal catalysts for oxygen reduction reaction: The demand-oriented engineering of active sites and structures, *Carbon Energy*, 2020, **2**, 561–581.

21 M. Gong, D.-Y. Wang, C.-C. Chen, B.-J. Hwang and H. Dai, A mini review on nickel-based electrocatalysts for alkaline hydrogen evolution reaction, *Nano Res.*, 2016, **9**, 28–46.

22 Q. Wang, R. Guo, Z. Wang, D. Shen, R. Yu, K. Luo, C. Wu and S. Gu, Progress in carbon-based electrocatalyst derived from biomass for the hydrogen evolution reaction, *Fuel*, 2021, **293**, 120440.

23 J. Zhu, L. Hu, P. Zhao, L. Y. S. Lee and K.-Y. Wong, Recent advances in electrocatalytic hydrogen evolution using nanoparticles, *Chem. Rev.*, 2019, **120**, 851–918.

24 S. A. Mirshokraee, M. Muhyuddin, R. Lorenzi, G. Tseberlidis, C. L. Vecchio, V. Baglio, E. Berretti, A. Lavacchi and C. Santoro, Litchi-derived platinum group metal-free electrocatalysts for oxygen reduction reaction and hydrogen evolution reaction in alkaline media, *SusMat*, 2023, **3**, 248–262.

25 S. H. Ahn, S. J. Hwang, S. J. Yoo, I. Choi, H.-J. Kim, J. H. Jang, S. W. Nam, T.-H. Lim, T. Lim and S.-K. Kim, Electrodeposited Ni dendrites with high activity and durability for hydrogen evolution reaction in alkaline water electrolysis, *J. Mater. Chem.*, 2012, **22**, 15153–15159.

26 Y. F. Xu, M. R. Gao, Y. R. Zheng, J. Jiang and S. H. Yu, Nickel/nickel (II) oxide nanoparticles anchored onto cobalt (IV) diselenide nanobelts for the electrochemical production of hydrogen, *Angewandte Chemie*, 2013, **125**, 8708–8712.

27 T. Sun, C. Zhang, J. Chen, Y. Yan, A. A. Zakhidov, R. H. Baughman and L. Xu, Three-dimensionally ordered macro-/mesoporous Ni as a highly efficient electrocatalyst for the hydrogen evolution reaction, *J. Mater. Chem. A*, 2015, **3**, 11367–11375.

28 S. A. Abbas, M. I. Iqbal, S.-H. Kim and K.-D. Jung, Catalytic activity of urchin-like Ni nanoparticles prepared by solvothermal method for hydrogen evolution reaction in alkaline solution, *Electrochim. Acta*, 2017, **227**, 382–390.

29 T. Sun, L. Xu, D. Wang and Y. Li, Metal organic frameworks derived single atom catalysts for electrocatalytic energy conversion, *Nano Res.*, 2019, **12**, 2067–2080.

30 L. Du, L. Luo, Z. Feng, M. Engelhard, X. Xie, B. Han, J. Sun, J. Zhang, G. Yin and C. Wang, Nitrogen–doped graphitized

carbon shell encapsulated NiFe nanoparticles: A highly durable oxygen evolution catalyst, *Nano Energy*, 2017, **39**, 245–252.

31 Y. Shen, Y. Zhou, D. Wang, X. Wu, J. Li and J. Xi, Nickel–copper alloy encapsulated in graphitic carbon shells as electrocatalysts for hydrogen evolution reaction, *Adv. Energy Mater.*, 2018, **8**, 1701759.

32 Y. Xu, Y. Liu, X. Zhang, K. Liu, R. Wang, Y. Yang, Z. Fang and J. Chen, Enhanced hydrogen evolution performance by nanoarchitectonics of Fe/Co alloy electrode beyond Fe/Co/Ni alloy electrode, *Int. J. Hydrogen Energy*, 2023, **48**, 757–765.

33 Y. Yang, Z. Lin, S. Gao, J. Su, Z. Lun, G. Xia, J. Chen, R. Zhang and Q. Chen, Tuning electronic structures of nonprecious ternary alloys encapsulated in graphene layers for optimizing overall water splitting activity, *ACS Catal.*, 2017, **7**, 469–479.

34 Y. Xiao, Y. Liu, Z. Tang, L. Wu, Y. Zeng, Y. Xu and Y. He, Porous Ni–Cr–Fe alloys as cathode materials for the hydrogen evolution reaction, *RSC Adv.*, 2016, **6**, 51096–51105.

35 L. Yu, T. Lei, B. Nan, J. Kang, Y. Jiang, Y. He and C. Liu, Mo doped porous Ni–Cu alloy as cathode for hydrogen evolution reaction in alkaline solution, *RSC Adv.*, 2015, **5**, 82078–82086.

36 A. Zaffora, F. Di Franco, D. Pupillo, B. Seminara, G. Tranchida and M. Santamaria, Highly active and stable NiCuMo electrocatalyst supported on 304 stainless steel porous transport layer for hydrogen evolution in alkaline water electrolyzer, *Adv. Sustainable Syst.*, 2023, **7**, 2200486.

37 A. C. Ferrari, J. C. Meyer, V. Scardaci, C. Casiraghi, M. Lazzeri, F. Mauri, S. Piscanec, D. Jiang, K. S. Novoselov and S. Roth, Raman spectrum of graphene and graphene layers, *Phys. Rev. Lett.*, 2006, **97**, 187401.

38 C. Beny-Bassez and J. Rouzaud, Characterization of carbonaceous materials by correlated electron and optical microscopy and Raman microspectroscopy, *Scanning Electron Microsc.*, 1984, **1985**, 11.

39 D. Testa, G. Zuccante, M. Muhyuddin, R. Landone, A. Scommegna, R. Lorenzi, M. Acciarri, E. Petri, F. Soavi and L. Poggini, Giving new life to waste cigarette butts: Transformation into platinum group metal-free electrocatalysts for oxygen reduction reaction in acid, neutral and alkaline Environment, *Catalysts*, 2023, **13**, 635.

40 O. Beyssac, J.-N. Rouzaud, B. Goffe, F. Brunet and C. Chopin, Graphitization in a high-pressure, low-temperature metamorphic gradient: A Raman microspectroscopy and HRTEM study, *Contrib. Mineral. Petrol.*, 2002, **143**, 19–31.

41 B. Wang, X. Li, B. Luo, J. Yang, X. Wang, Q. Song, S. Chen and L. Zhi, Pyrolyzed bacterial cellulose: a versatile support for lithium ion battery anode materials, *Small*, 2013, **9**, 2399–2404.

42 L. M. Malard, M. H. Guimarães, D. L. Mafra and A. Jorio, Group-theory analysis of electrons and phonons in N-layer graphene systems, *Phys. Rev. B: Condens. Matter Mater. Phys.*, 2009, **79**, 125426.

43 L. G. Cançado, A. Jorio, E. M. Ferreira, F. Stavale, C. A. Achete, R. B. Capaz, M. V. D. O. Moutinho, A. Lombardo, T. Kulmala and A. C. Ferrari, Quantifying defects in graphene *via* Raman spectroscopy at different excitation energies, *Nano Lett.*, 2011, **11**, 3190–3196.

44 C. Casiraghi, S. Pisana, K. Novoselov, A. K. Geim and A. Ferrari, Raman fingerprint of charged impurities in graphene, *Appl. Phys. Lett.*, 2007, **91**, 233108.

45 K. Saenger, J. Tsang, A. Bol, J. Chu, A. Grill and C. Lavoie, In situ x-ray diffraction study of graphitic carbon formed during heating and cooling of amorphous-C/Ni bilayers, *Appl. Phys. Lett.*, 2010, **96**, 153105.

46 M. Hu, J. Reboul, S. Furukawa, N. L. Torad, Q. Ji, P. Srinivasu, K. Ariga, S. Kitagawa and Y. Yamauchi, Direct carbonization of Al-based porous coordination polymer for synthesis of nanoporous carbon, *J. Am. Chem. Soc.*, 2012, **134**, 2864–2867.

47 N. Bozovic, I. Bozovic and J. Misewich, X-ray nanocrystallography of individual carbon nanotubes, *Nano Lett.*, 2008, **8**, 4477–4482.

48 D. Graf, F. Molitor, K. Ensslin, C. Stampfer, A. Jungen, C. Hierold and L. Wirtz, Spatially resolved Raman spectroscopy of single-and few-layer graphene, *Nano Lett.*, 2007, **7**, 238–242.

49 L. Zhang, Y. Jia, X. Yan and X. Yao, Activity origins in nanocarbons for the electrocatalytic hydrogen evolution reaction, *Small*, 2018, **14**, 1800235.

50 M. Muhyuddin, N. Zocche, R. Lorenzi, C. Ferrara, F. Poli, F. Soavi and C. Santoro, Valorization of the inedible pistachio shells into nanoscale transition metal and nitrogen codoped carbon-based electrocatalysts for hydrogen evolution reaction and oxygen reduction reaction, *Mater. Renewable Sustainable Energy*, 2022, **11**, 131–141.

51 A. S. Rajan, S. Sampath and A. K. Shukla, An in situ carbon-grafted alkaline iron electrode for iron-based accumulators, *Energy Environ. Sci.*, 2014, **7**, 1110–1116.

52 Z. Yang, Z. Yu, H. Wei, X. Xiao, Z. Ni, B. Chen, Y. Deng, S. N. Habisreutinger, X. Chen and K. Wang, Enhancing electron diffusion length in narrow-bandgap perovskites for efficient monolithic perovskite tandem solar cells, *Nat. Commun.*, 2019, **10**, 4498.

53 S. Sun, G. Zhang, N. Gauquelin, N. Chen, J. Zhou, S. Yang, W. Chen, X. Meng, D. Geng and M. N. Banis, Single-atom catalysis using Pt/graphene achieved through atomic layer deposition, *Sci. Rep.*, 2013, **3**, 1775.

54 R. Gokhale, Y. Chen, A. Serov, K. Artyushkova and P. Atanassov, Direct synthesis of platinum group metal-free Fe-NC catalyst for oxygen reduction reaction in alkaline media, *Electrochem. Commun.*, 2016, **72**, 140–143.

55 B. Ravel and M. Newville, ATHENA, ARTEMIS, HEPHAESTUS: data analysis for X-ray absorption spectroscopy using IFEFFIT, *J. Synchrotron Radiat.*, 2005, **12**, 537–541.

56 G. Rossi, F. d'Acapito, L. Amidani, F. Boscherini and M. Pedio, Local environment of metal ions in phthalocyanines: K-edge X-ray absorption spectra, *Phys. Chem. Chem. Phys.*, 2016, **18**, 23686–23694.

57 Q. Chang, Y. Liu, J.-H. Lee, D. Ologunagba, S. Hwang, Z. Xie, S. Kattel, J. H. Lee and J. G. Chen, Metal-coordinated phthalocyanines as platform molecules for understanding isolated metal sites in the electrochemical reduction of CO2, *J. Am. Chem. Soc.*, 2022, **144**, 16131–16138.

58 J. Guo, X. Yan, Q. Liu, Q. Li, X. Xu, L. Kang, Z. Cao, G. Chai, J. Chen and Y. Wang, The synthesis and synergistic catalysis of iron phthalocyanine and its graphene-based axial complex for enhanced oxygen reduction, *Nano Energy*, 2018, **46**, 347–355.

59 V. Bambagioni, C. Bianchini, J. Filippi, A. Lavacchi, W. Oberhauser, A. Marchionni, S. Moneti, F. Vizza, R. Psaro and V. Dal Santo, Single-site and nanosized Fe–Co electrocatalysts for oxygen reduction: Synthesis, characterization and catalytic performance, *J. Power Sources*, 2011, **196**, 2519–2529.

60 J. Zang, F. Wang, Q. Cheng, G. Wang, L. Ma, C. Chen, L. Yang, Z. Zou, D. Xie and H. Yang, Cobalt/zinc dual-sites coordinated with nitrogen in nanofibers enabling efficient and durable oxygen reduction reaction in acidic fuel cells, *J. Mater. Chem. A*, 2020, **8**, 3686–3691.

61 A. Alsudairi, J. Li, N. Ramaswamy, S. Mukerjee, K. Abraham and Q. Jia, Resolving the iron phthalocyanine redox transitions for ORR catalysis in aqueous media, *J. Phys. Chem. Lett.*, 2017, **8**, 2881–2886.

62 J. Ding, H. Yang, S. Zhang, Q. Liu, H. Cao, J. Luo and X. Liu, Advances in the electrocatalytic hydrogen evolution reaction by metal nanoclusters-based materials, *Small*, 2022, **18**, 2204524.

63 J. Salmones, J. Wang, M. Valenzuela, E. Sánchez and A. Garcia, Pore geometry influence on the deactivation behavior of Ni-based catalysts for simultaneous production of hydrogen and nanocarbon, *Catal. Today*, 2009, **148**, 134–139.

64 A. Venugopal, S. N. Kumar, J. Ashok, D. H. Prasad, V. D. Kumari, K. Prasad and M. Subrahmanyam, Hydrogen production by catalytic decomposition of methane over Ni/SiO2, *Int. J. Hydrogen Energy*, 2007, **32**, 1782–1788.

65 T. Choudhary, C. Sivadinarayana, C. C. Chusuei, A. Klinghoffer and D. Goodman, Hydrogen production via catalytic decomposition of methane, *J. Catal.*, 2001, **199**, 9–18.

66 S. K. Saraswat and K. Pant, Thermo catalytic decomposition of methane: A novel approach to COx free hydrogen and carbon nanotubes production over Ni/SiO2 catalyst, *Energy*, 2012, **1**, 2.

67 S. Karimi, F. Bibak, F. Meshkani, A. Rastegarpanah, J. Deng, Y. Liu and H. Dai, Promotional roles of second metals in catalyzing methane decomposition over the Ni-based catalysts for hydrogen production: A critical review, *Int. J. Hydrogen Energy*, 2021, **46**, 20435–20480.

68 L. Hu, J. Shi, Z. Peng, Z. Zheng, H. Dong and T. Wang, A high-density nickel–cobalt alloy embedded in nitrogen-

© 2023 The Author(s). Co-published by the Institute of Process Engineering, Chinese Academy of Sciences and the Royal Society of Chemistry

Ind. Chem. Mater., 2023, **1**, 343–359 | **357**

doped carbon nanosheets for the hydrogen evolution reaction, *Nanoscale*, 2022, **14**, 6202–6211.

69 Z. Zhang, L. Cong, Z. Yu, L. Qu and W. Huang, Facile synthesis of Fe–Ni bimetallic N-doped carbon framework for efficient electrochemical hydrogen evolution reaction, *Mater. Today Energy*, 2020, **16**, 100387.

70 Z. Zhang, L. Cong, Z. Yu, L. Qu, M. Qian and W. Huang, FeNiMo trimetallic nanoparticles encapsulated in carbon cages as efficient hydrogen evolution reaction electrocatalysts, *Mater. Adv.*, 2020, **1**, 54–60.

71 H. Wang, H.-W. Lee, Y. Deng, Z. Lu, P.-C. Hsu, Y. Liu, D. Lin and Y. Cui, Bifunctional non-noble metal oxide nanoparticle electrocatalysts through lithium-induced conversion for overall water splitting, *Nat. Commun.*, 2015, **6**, 7261.

72 C. Zhu, A. L. Wang, W. Xiao, D. Chao, X. Zhang, N. H. Tiep, S. Chen, J. Kang, X. Wang and J. Ding, In situ grown epitaxial heterojunction exhibits high-performance electrocatalytic water splitting, *Adv. Mater.*, 2018, **30**, 1705516.

73 X. Wang, W. Li, D. Xiong, D. Y. Petrovykh and L. Liu, Bifunctional nickel phosphide nanocatalysts supported on carbon fiber paper for highly efficient and stable overall water splitting, *Adv. Funct. Mater.*, 2016, **26**, 4067–4077.

74 C. Lei, Y. Wang, Y. Hou, P. Liu, J. Yang, T. Zhang, X. Zhuang, M. Chen, B. Yang and L. Lei, Efficient alkaline hydrogen evolution on atomically dispersed Ni–N x Species anchored porous carbon with embedded Ni nanoparticles by accelerating water dissociation kinetics, *Energy Environ. Sci.*, 2019, **12**, 149–156.

75 Z. Bai, S. Li, J. Fu, Q. Zhang, F. Chang, L. Yang, J. Lu and Z. Chen, Metal-organic framework-derived Nickel Cobalt oxysulfide nanocages as trifunctional electrocatalysts for high efficiency power to hydrogen, *Nano Energy*, 2019, **58**, 680–686.

76 K. E. Salem, A. A. Saleh, G. E. Khedr, B. S. Shaheen and N. K. Allam, Unveiling the optimal interfacial synergy of plasma-modulated trimetallic Mn-Ni-Co phosphides: Tailoring deposition ratio for complementary water splitting, *Energy Environ. Mater.*, 2023, **6**, e12324.

77 W. Orellana, C. Z. Loyola, J. F. Marco and F. Tasca, Evidence of carbon-supported porphyrins pyrolyzed for the oxygen reduction reaction keeping integrity, *Sci. Rep.*, 2022, **12**, 8072.

78 E. Giordano, E. Berretti, L. Capozzoli, A. Lavacchi, M. Muhyuddin, C. Santoro, I. Gatto, A. Zaffora and M. Santamaria, Boosting DMFC power output by adding sulfuric acid as a supporting electrolyte: Effect on cell performance equipped with platinum and platinum group metal-free cathodes, *J. Power Sources*, 2023, **563**, 232806.

79 C. Lo Vecchio, A. S. Aricò and V. Baglio, Application of low-cost Me-NC (Me= Fe or Co) electrocatalysts derived from edta in direct methanol fuel cells (DMFCs), *Materials*, 2018, **11**, 1193.

80 C. L. Vecchio, A. S. Aricò, G. Monforte and V. Baglio, EDTA-derived CoNC and FeNC electro-catalysts for the oxygen reduction reaction in acid environment, *Renewable Energy*, 2018, **120**, 342–349.

81 S. Chen, F. Bi, K. Xiang, Y. Zhang, P. Hao, M. Li, B. Zhao and X. Guo, Reactive template-derived CoFe/N-doped carbon nanosheets as highly efficient electrocatalysts toward oxygen reduction, oxygen evolution, and hydrogen evolution, *ACS Sustainable Chem. Eng.*, 2019, **7**, 15278–15288.

82 R. Mercado, C. Wahl, J. En Lu, T. Zhang, B. Lu, P. Zhang, J. Q. Lu, A. L. Allen, J. Z. Zhang and S. Chen, Nitrogen-doped porous carbon cages for electrocatalytic reduction of oxygen: Enhanced performance with iron and cobalt dual metal centers, *ChemCatChem*, 2020, **12**, 3230–3239.

83 X.-W. Song, S. Zhang, H. Zhong, Y. Gao, L. A. Estudillo-Wong, N. Alonso-Vante, X. Shu and Y. Feng, FeCo nanoalloys embedded in nitrogen-doped carbon nanosheets/bamboo-like carbon nanotubes for the oxygen reduction reaction, *Inorg. Chem. Front.*, 2021, **8**, 109–121.

84 S. H. Liu and H. C. Kuo, Core-shell FeCo N-doped biocarbons as stable electrocatalysts for oxygen reduction reaction in fuel cells, *Int. J. Energy Res.*, 2021, **45**, 8285–8295.

85 Y. Zhou, Y. Zhang, X. Xu, S. Zhao, Z. Guo, K.-H. Wu, C. Tan and Z. Wang, Bimetallic metal-organic framework derived metal-carbon hybrid for efficient reversible oxygen electrocatalysis, *Front. Chem.*, 2019, **7**, 747.

86 E. Gul, L. Riva, H. K. Nielsen, H. Yang, H. Zhou, Q. Yang, Ø. Skreiberg, L. Wang, M. Barbanera and M. Zampilli, Substitution of coke with pelletized biocarbon in the European and Chinese steel industries: An LCA analysis, *Appl. Energy*, 2021, **304**, 117644.

87 A. Serov, K. Artyushkova, N. I. Andersen, S. Stariha and P. Atanassov, Original mechanochemical synthesis of non-platinum group metals oxygen reduction reaction catalysts assisted by sacrificial support method, *Electrochim. Acta*, 2015, **179**, 154–160.

88 N. Ramaswamy and S. Mukerjee, Influence of inner-and outer-sphere electron transfer mechanisms during electrocatalysis of oxygen reduction in alkaline media, *J. Phys. Chem. C*, 2011, **115**, 18015–18026.

89 A. Di Cicco, G. Aquilanti, M. Minicucci, E. Principi, N. Novello, A. Cognigni and L. Olivi, Novel XAFS capabilities at ELETTRA synchrotron light source, *J. Phys.: Conf. Ser.*, 2009, **190**, 012043.

90 M. Muhyuddin, A. Friedman, F. Poli, E. Petri, H. Honig, F. Basile, A. Fasolini, R. Lorenzi, E. Berretti and M. Bellini, Lignin-derived bimetallic platinum group metal-free oxygen reduction reaction electrocatalysts for acid and alkaline fuel cells, *J. Power Sources*, 2023, **556**, 232416.

91 M. Muhyuddin, D. Testa, R. Lorenzi, G. M. Vanacore, F. Poli, F. Soavi, S. Specchia, W. Giurlani, M. Innocenti and L. Rosi, Iron-based electrocatalysts derived from scrap tires for oxygen reduction reaction: Evolution of synthesis-structure-performance relationship in acidic, neutral and alkaline media, *Electrochim. Acta*, 2022, **433**, 141254.

92 G. Jerkiewicz, Standard and reversible hydrogen electrodes: Theory, design, operation, and applications, *ACS Catal.*, 2020, **10**, 8409–8417.

93 M. Muhyuddin, J. Filippi, L. Zoia, S. Bonizzoni, R. Lorenzi, E. Berretti, L. Capozzoli, M. Bellini, C. Ferrara and A. Lavacchi, Waste face surgical mask transformation into crude oil and nanostructured electrocatalysts for fuel cells and electrolyzers, *ChemSusChem*, 2022, **15**, e202102351.

94 S. A. Mirshokraee, M. Muhyuddin, R. Morina, L. Poggini, E. Berretti, M. Bellini, A. Lavacchi, C. Ferrara and C. Santoro, Upcycling of waste lithium-cobalt-oxide from spent batteries into electrocatalysts for hydrogen evolution reaction and oxygen reduction reaction: A strategy to turn the trash into treasure, *J. Power Sources*, 2023, **557**, 232571.

© 2023 The Author(s). Co-published by the Institute of Process Engineering, Chinese Academy of Sciences and the Royal Society of Chemistry

Ind. Chem. Mater., 2023, **1**, 343–359 | **359**